Distinct thermodynamic signature of oligomer generation in the aggregation of the amyloid-β peptide

Supplementary Information

Samuel I. A. Cohen[1†], Risto Cukalevski[2†], Thomas. C. T. Michaels[1], Anđela Šarić[1,3], Mattias Törnquist[2], Michele Vendruscolo[1], Christopher M. Dobson[1], Alexander K. Buell[4], Tuomas P. J. Knowles[1*], and Sara Linse[2*]

[1]*Department of Chemistry, University of Cambridge, Lensfield Road, Cambridge, CB2 1EW, UK*
[2]*Department of Biochemistry and Structural Biology, Lund University, Box 124, SE221 00 Lund, Sweden*
[3]*Department of Physics and Astronomy, Institute for the Physics of Living Systems, University College London, London WC1E 6BT, UK*
[4]*Institute of Physical Biology, University of Duesseldorf, 40225 Duesseldorf, Germany*

[†] these authors contributed equally

[*]to whom correspondence should be addressed: tpjk2@cam.ac.uk or sara.linse@biochemistry.lu.se

Contents

1. Supplementary Note
Analysis of the temperature dependence of the individual microscopic steps involved in secondary nucleation

1.1 Objective and introduction

The aim of this supplementary note is to decompose the overall temperature dependence of the secondary nucleation rate, determined experimentally as described in the main text, in terms of the temperature dependence of its constituent microscopic steps, namely the adsorption of monomers onto the fibril surface and the subsequent surface-catalysed conformational conversion leading to nucleus formation and detachment. Using these results, we construct the energy landscape of both processes as a function of the concentration of monomers in solution.

In the main text, we have applied a kinetic analysis approach based on master equations to fit the time course of the aggregate mass concentration measured at different temperatures. This analysis allowed us to extract the temperature dependence of the overall rate constant for secondary fibril nucleation, $k_2(T)$. The fact that $k_2(T)$ is a coarse-grained quantity that captures the overall nucleation step from monomers directly to aggregates naturally motivates the following question: does the temperature dependence of $k_2(T)$ provide any insights into the temperature dependence of the constituent microscopic steps of secondary nucleation, in particular the initial monomer adsorption step and the subsequent reaction on the fibril surface?

The main challenge in addressing this question comes from the fact that fibril nucleation processes are highly complex phenomena involving the concurrent making and breaking of many hundreds of bonds between the multiple molecular species present. This challenge is analogous to that encountered in protein folding dynamics, which, even for the smallest proteins, involve rearranging a large number of interactions between the constituent atoms. In the context of protein folding dynamics, much progress has been made by setting aside the full complexity of the problem and modeling the process as a diffusive passage over a free energy barrier along a potential energy landscape with just a few important coordinates. Such diffusive dynamics processes are the focus of Kramers reaction rate theory, which has therefore become a powerful approach for analyzing protein folding dynamics. In the following, we aim at applying Kramers reaction theory to study the problem of secondary fibril nucleation as a multi-molecular reaction governed by diffusive dynamics and, in this manner, extract information about the temperature dependence of its constituents microscopic steps.

This material is organized as follows. In Section 1.2, we review Kramers theory of diffusive dynamics. We study the general situation of a double-well potential landscape first and then discuss generalizations to multi-well potential landscapes. In Section 1.3, we discuss the strategy for analyzing the temperature dependence of secondary fibril nucleation rates using Kramers rate theory. Finally in Section 1.4, we apply these results to the analysis of experimental data and construct the potential energy landscape for secondary fibril nucleation as a function of the concentration of monomers in solution.

1.2 Diffusive dynamics and Kramers rate theory

In what follows we review some key results from Kramers theory of diffusive reactions which will represent the starting point for the temperature analysis discussed in Sections 1.3 and 1.4 and summarized in Figs. 3–5 in the main text. We will first study a model example of a diffusive reaction governed by a single free energy barrier. We will then extend the framework to diffusive reactions in an energy landscape with multiple barriers and show how in this case the reaction rate depends only on the highest free energy barrier, measured relative to the starting point of the reaction.

1.2.1 Kramers rate theory for a double-well potential

Consider a one-dimensional double-well potential landscape $G(x)$ having local minima in correspondence of the reaction coordinates x_1 and x_2 (see Supplementary Fig. 5a). The key question is: how long does it take on average for the system to diffuse from the minimum x_1 to the other one x_2? A rigorous answer to this problem is given in terms of the first-hitting time of the point x_2, starting in x_1: $\tau(x_1 \to x_2)$. Clearly, because the diffusion process from x_1 to x_2 is random, $\tau(x_1 \to x_2)$ is a random variable. However, in the limit when the free energy barrier is much bigger than the thermal energy ($\varepsilon = RT/G \ll 1$), its average can be computed and satisfies the (Eyring)-Kramers law [1]:

$$\langle \tau(x_1 \to x_2) \rangle \simeq \frac{2\pi}{\sqrt{G''(x_1)|G''(x^\star)|}} e^{[G(x^\star) - G(x_1)]/RT}$$
$$= C \, e^{\Delta G^\ddagger/RT}. \tag{S1}$$

Due to the equivalence between average first exit times from a potential well and the inverse of the associated Kramers escape rate r (see Appendix), we can invert Eq. S1 to find the escape rate from x_1:

$$r = \frac{1}{\langle \tau(x_1 \to x_2) \rangle} \simeq A \, e^{-\Delta G^\ddagger/RT}. \tag{S2}$$

Thus, the rate at which the system diffuses from x_1 to x_2 is given by a prefactor A (which depends on the curvatures $G''(x_1)$ and $G''(x^*)$ of the potential landscape at x_1 and x^*, respectively) multiplied by the negative exponential of the highest free energy point measured relatively to the starting point.

1.2.2 Kramers rate theory for multi-well potentials

When the potential landscape has multiple local minima, can the escape rate still be written in the form of Eyring equation? The answer to this question is that the escape rate satisfies Eyring equation provided that the local minima satisfy certain ordering conditions. In particular, it has been demonstrated [2] that for a multi-well potential landscape having local minima at $x_1, x_2, \cdots, x_n$ there exists an ordering $\prec$ of these local minima (the ordering is obtained by ordering the minima from deepest to shallowest) so that the expectation value for the average escape time from x_k to the set $\mathcal{M}_k = \{x_j | x_j \prec x_k\}$ satisfies Kramers formula

$$\langle \tau(x_k \to \mathcal{M}_k) \rangle \simeq C e^{[H(x_k, \mathcal{M}_k) - G(x_k)]/RT}, \tag{S3}$$

where the argument of the exponential function $H(\xi, \omega)$ is called the communication height and is defined by

$$H(\xi, \omega) = \inf_{\gamma: \xi \to \omega} \left(\sup_{\eta \in \gamma} G(\eta) \right) \tag{S4}$$

where the infimum is taken over all curves γ going from ξ to ω along the potential landscape. Note that there is a single point $\eta^\star$ realizing the supremum in Eq. S4; this point defines the relevant saddle point between ξ and ω and determines the relevant free energy barrier controlling the escape rate.

Let us consider as an example of the application of this theorem the energy landscape in Supplementary Fig. 5b. The minima in the figure are ordered from the deepest to the shallowest as $x_3 \prec x_1 \prec x_2$. Thus, according to the above theorem, the average first-hitting time of x_3 starting from x_1 satisfies an Eyring equation. To find the relevant argument of the exponential, we compute the communication height between x_1 and x_3

$$H(x_1, x_3) = \inf_{\gamma: x_1 \to x_3} \left(\sup_{\eta \in \gamma} G(\eta) \right). \tag{S5}$$

As there is only one curve γ connecting x_1 to x_3, $H(x_1, x_3)$ necessarily corresponds to the maximum of $G(x)$ between x_1 and x_3:

$$H(x_1, x_3) = G(x^\star), \tag{S6}$$

3

where $x^\star$ is the point indicated in Supplementary Fig. 5b. Thus,

$$\langle \tau(x_1 \to x_3) \rangle \simeq C e^{[G(x^\star) - G(x_1)]/RT} = C e^{\Delta G^\ddagger / RT} \tag{S7}$$

and the associated escape rate is

$$r = \frac{1}{\langle \tau(x_1 \to x_3) \rangle} \simeq A e^{-\Delta G^\ddagger / RT}. \tag{S8}$$

Thus, the rate for diffusing from x_1 to x_3 only depends on the highest free energy barrier ($\Delta G^\ddagger$) measured relatively to the starting point x_1. Finally we highlight that Eq. S8 does not apply when the ordering of the minima x_1 and x_2 is reversed. We note however that this condition is satisfied for secondary nucleation at $c = 1\mu M$, as discussed in what follows.

1.3 General strategy to analyse secondary nucleation

1.3.1 Kinetic approach

The standard procedure of kinetic analysis based on closed-form solutions for the aggregate mass concentration allows us to determine the overall temperature-dependent rate constant for secondary nucleation, $k_2(T)$, from a global fit of aggregation kinetics at different temperatures [3]. The total rate of secondary nucleation is then given by:

$$r(T, c) = k_2(T) c^{n_2}, \tag{S9}$$

where c is the monomer concentration, n_2 is the reaction order. Note that this expression tacitly assumes that the concentration c is sufficiently low that the process of secondary nucleation is not saturated [4].

1.3.2 Insights from simulations

From computer simulations of the process, supported by biosensing experiments, we infer [5] that the rate of secondary nucleation depends on the fibril surface coverage $\theta = c/(K_D + c)$, where $1/K_D$ is the monomer-surface binding constant. Note that the fibril surface coverage θ is dependent both on the monomer concentration and temperature, hence K_D is temperature dependent. The rate of secondary nucleation can then be written in the form:

$$r(T, c) = k(T) \theta(T, c)^N, \tag{S10}$$

where N is related to the size of the nucleating oligomer (see Ref. [5], page 878, second paragraph). Note that $k(T)$ and N are in principle distinct from the parameters $k_2(T)$ and n_2 in Eq. S9.

1.3.3 Matching theory with simulations

How are the theoretical kinetic approach and the approach based on computer simulations discussed in the previous two sections related to each other? At low peptide concentrations ($c \lesssim K_D$), the fibril surface is unsaturated, and the surface coverage can be approximated by a linear function of the monomer concentration

$$\theta(T, c) = \frac{c/K_D(T)}{1 + c/K_D(T)} \approx \frac{c}{K_D(T)}. \tag{S11}$$

In this regime, Eq. S10 can be re-written as

$$r(T, c) = k(T) \theta(T, c)^N \approx \frac{k(T)}{K_D(T)^N} c^N. \tag{S12}$$

In this regime, the expression for the rate of secondary nucleation, Eq. S12, recovers Eq. S9. In particular, comparing the two equations allows us to make the following identification:

$$k_2(T) = k(T) \alpha(T)^N, \text{ hence } N = n_2, \tag{S13}$$

4

where

$$\alpha(T) = \frac{1}{K_D(T)} \tag{S14}$$

is a parameter that captures the temperature dependence of the surface coverage. Note that to obtain the second equality in Eq. S13 we have exploited the fact that N is constant, as observed both in kinetic fitting and computer simulations.

Equation S13 is a key result of this section. It shows that the overall temperature dependence of the rate of secondary nucleation, expressed by $k_2(T)$, can be decomposed into the temperature-dependence of the individual microscopic steps: the surface coverage, $\alpha = \theta/c$, and the temperature-dependence of the surface-catalysed nucleation step, $k(T)$.

1.4 Application to the experimental data

1.4.1 Strategy

The experimental kinetic data is collected in the 2-10 μM range of monomer concentrations, where the fibril surfaces are to a very good approximation unsaturated at all temperatures [4]. In this regime, we have shown that the rate of secondary nucleation can be expressed as

$$r(T,c) = k(T)\theta(T,c)^{n_2}, \tag{S15}$$

with

$$k(T) = \frac{k_2(T)}{\alpha(T)^{n_2}}, \tag{S16}$$

or, equivalently,

$$k_2(T) = k(T)\alpha(T)^{n_2}. \tag{S17}$$

This is a central relation that we will use to extract the temperature dependence of the individual mechanistic steps of the secondary nucleation process. In particular, from the analysis of kinetic data we can extract the temperature dependence of the overall rate constant for secondary nucleation, $k_2(T)$, as explained in the main text. Moreover, the temperature dependence of the surface coverage, and thus of the parameter $\alpha(T)$, can be obtained from SPR experiments. From the availability of the temperature dependencies of $k_2(T)$ and $\alpha(T)$, we can evaluate $k(T)$ using Eq. S16. Obtaining $k(T)$ in such a way will give us information about the temperature-dependence of the surface-catalysed nucleation step, a necessary ingredient for constructing the energy landscape. In what follows we discuss in detail how we obtain $k(T)$.

1.4.2 Experimental temperature dependence of the overall rate constant $k_2(T)$

From the kinetic analysis discussed in the main text, we infer that $N = 2$ and the overall temperature-dependent rate constant for secondary nucleation, $k_2(T)$, reads:

$$k_2(T = 293.15K) = 2.7 \cdot 10^4 \text{ M}^{-2}\text{s}^{-1}$$
$$k_2(T = 303.15K) = 2.2 \cdot 10^4 \text{ M}^{-2}\text{s}^{-1}$$
$$k_2(T = 313.15K) = 1.8 \cdot 10^4 \text{ M}^{-2}\text{s}^{-1}.$$

1.4.3 Experimental temperature dependence of the surface coverage $\alpha(T)$

The monomer-fibril binding constant, $1/K_D(T)$, is obtained from fitting the SPR experimental data to the Langmuir isotherm. From Eq. S14 we find the following $\alpha(T)$:

$$\alpha(T = 293.15K) = 9.1 \cdot 10^4 \text{ M}^{-1}$$
$$\alpha(T = 303.15K) = 3.8 \cdot 10^4 \text{ M}^{-1}$$
$$\alpha(T = 313.15K) = 1.6 \cdot 10^4 \text{ M}^{-1}.$$

1.4.4 Temperature dependence of the surface-catalysed nucleation $k(T)$

From the measured values of $k_2(T)$ and $\alpha(T)$, using Eq. S16, we are now in a position to determine the rate constant of the surface catalysed step $k(T)$:

$$k(T = 293.15K) = 3.2 \cdot 10^{-6} \text{ s}^{-1}$$
$$k(T = 303.15K) = 1.5 \cdot 10^{-5} \text{ s}^{-1}$$
$$k(T = 313.15K) = 7.3 \cdot 10^{-5} \text{ s}^{-1}.$$

It is apparent that $k(T)$ exhibits a positive and a relatively strong temperature dependence (with a 20-fold increase over 20^oC).

1.5 Building the energy landscape from $k_2(T)$, $\alpha(T)$ and $k(T)$

1.5.1 Thermodynamics of monomer adsorption onto the fibril

We first use $\alpha(T)$ to determine the thermodynamics of the adsorption step unto the fibril. According to the Clausius-Clapeyron equation, the enthalpy of monomer adsorption onto the fibrils surface can be evaluated as:

$$\frac{\Delta H_{\text{ads}}}{R} = \left(\frac{\partial \ln(K_d)}{\partial (1/T)} \right)_\theta = -\frac{\partial \ln(\alpha(T))}{\partial (1/T)}. \tag{S18}$$

The value obtained using $\alpha(T)$ from the previous section is:

$$\Delta H_{\text{ads}} = -67 \text{ kJmol}. \tag{S19}$$

Combining this quantity and $K_D(T)$ also allows us to directly access the adsorption entropy change via:

$$\Delta G_{\text{ads}} = -RT \ln(c^\ominus/K_D) + RT \ln(c/c^\ominus)$$
$$= \Delta H_{\text{ads}} - T\Delta S_{\text{ads}}, \tag{S20}$$

where c is the monomer concentration in solution and $c^\ominus = 1$ M . At $T = 298$ K and $c = 1$ M the calculation gives

$$\Delta G_{\text{ads}} = -27 \text{ kJmol}, \quad T\Delta S_{\text{ads}} = -40 \text{ kJmol}. \tag{S21}$$

However, at $T = 298$ K and $c = 1$ μM the adsorption free energy change is positive

$$\Delta G_{\text{ads}} = 7 \text{ kJmol}, \quad T\Delta S_{\text{ads}} = -74 \text{ kJmol}. \tag{S22}$$

1.5.2 Evaluation of the post-adsorption enthalpic nucleation barrier $\Delta H_2^\ddagger$

We next use the temperature dependence of the surface-catalysed nucleation, $k(T)$, to determine the thermodynamics of this step following monomer adsorption onto the fibril. The enthalpy of activation of the surface-catalysed nucleation step can be evaluated as:

$$\frac{\Delta H_2^\ddagger}{R} = \frac{\partial \ln(k(T))}{\partial (1/T)}. \tag{S23}$$

Using the extracted values for $k(T)$, we obtain a value of $\Delta H_2^\ddagger = 119$ kJ/mol, which is comparable to the enthalpic barrier of primary nucleation.

1.5.3 Overall enthalpic barrier for secondary nucleation, $\Delta H^\ddagger$

In the main text the enthalpic barrier of the secondary nucleation process has been extracted from the temperature dependence of the overall nucleation step, $k_2(T)$, and its value was $\Delta H^\ddagger = (-11 \pm 7)$ kJ/mol. As a consistency check, we now verify that this value agrees with the value obtained from combining the adsorption enthalpy (Eq. S19) and the post-adsorption enthalpic nucleation barrier (Eq. S23). Combining these two contributions gives the weak overall enthalpic barrier for secondary nucleation:

$$\Delta H^\ddagger = R\frac{\partial \ln(k(T))}{\partial(1/T)} + NR\frac{\partial \ln(\alpha(T))}{\partial(1/T)}$$
$$= \Delta H_2^\ddagger + 2\Delta H_{\text{ads}} = -15 \text{ kJ/mol}, \tag{S24}$$

a value which agrees well with the enthalpic barrier $\Delta H^\ddagger = (-11 \pm 7)$ kJ/mol determined directly from the temperature-dependence of $k_2(T)$.

1.5.4 Overall entropic and free energy barriers for secondary nucleation

The temperature-dependence of the rate constant for secondary nucleation is given by Kramers formula

$$k_2(T) = A\, e^{-\Delta G^\ddagger/RT}, \tag{S25}$$

where $\Delta G^\ddagger$ corresponds to the highest free energy point along the potential landscape. To determine the free energy of activation for the secondary nucleation, an estimate of the prefactor A is needed. For fibril elongation, which is effectively a unimolecular reaction, we have shown that $A \sim N_A D r_{\text{eff}}$, where N_A is the Avogadro's constant [6, 7]. For the nucleation processes, we choose also to work with a reference value of the frequency pre-factor corresponding to an attempted frequency from free diffusive motion [6, 7]. Since, inevitably, we do not have complete information about diffusion along the reaction coordinate for the nucleation processes, we partition all of the missing information into the free energy barrier in the rate equation. Other choices of partitionings are equally possible (for example, accounting for the adsorption process in the pre-factor); one advantage of our choice of partitioning is that the pre-factor can be readily estimated. More generally, in this type of analysis the kinetic pre-factor and the free energy barrier are never independent, and the latter is only meaningful if stated together with the corresponding pre-factor. Furthermore, the precise value of the frequency pre-factor enters only as a logarithmic correction to the entropies of activation; hence a difference of a factor of 10 in the pre-factor results in a change in the entropy and free energy activation parameters for the nucleation processes by only $RT \log(10) = 5.7$ kJ mol^{-1}.

As the rate of secondary nucleation depends on the monomer concentration with a power $n_2 = 2$, to obtain a quantity with the same dimensions as k_2 we infer $A = N_A D r_{\text{eff}}/c$. Hence, we obtain

$$k_2(T) = \frac{N_A D r_{\text{eff}}}{c} e^{-\Delta H^\ddagger/RT - \Delta S^\ddagger/R}, \tag{S26}$$

which can be rearranged to give:

$$T\Delta S^\ddagger(c) = RT \ln\left(\frac{k_2 c}{N_A D r_{\text{eff}}}\right) + \Delta H^\ddagger. \tag{S27}$$

We have previously established estimates for the radius of the effective reaction volume $r_{\text{eff}} \sim 3\cdot 10^{-11}$m and the diffusion coefficient $D \sim 10^{-9}$m^{2}s^{-1} for Aβ in the context of fibril elongation [6, 7]. It is interesting to note that the rate determining step of secondary nucleation may involve the reaction between a fibril-bound monomer and a free monomer, or between two fibril-bound monomers. The former case would be similar to elongation, whereas the latter scenario may have a reduced prefactor corresponding to the diffusion of a bound monomer along the fibril surface. Such a process can be modeled as diffusion in a rough potential and the reduction in diffusion coefficient compared to

free diffusion depends on the amplitude of the roughness [8]; however, for a significant reduction in the pre-factor to occur, the roughness features would have to be several $k_B T$.

At $T = 298$ K and $c = 1$ M, the calculation gives:

$$\Delta G^{\ddagger} = 16 \text{ kJmol}, \quad T\Delta S^{\ddagger} = -27 \text{ kJmol}, \tag{S28}$$

while at $T = 298$ K and $c = 1$ μM, we obtain:

$$\Delta G^{\ddagger} = 32 \text{ kJmol}, \quad T\Delta S^{\ddagger} = -43 \text{ kJmol}. \tag{S29}$$

Supplementary Fig. 6 summarizes graphically the results of the energy landscape of secondary nucleation analysis discussed here, and places it in contrast with the energy landscape of primary nucleation, discussed in the main text.

1.5.5   Why does the highest free energy barrier follow the monomer adsorption step?

It is important at this point to comment on our assumption that the highest free energy barrier in the system takes place after the monomer adsorption onto the surface, and not before. From the kinetic measurements of the secondary nucleation of Aβ40 [4] it is known that the rate of the secondary nucleation saturates in the micromolar range of peptide concentrations, which correlates with the saturation of the fibril surface coverage by monomeric peptides in the same concentration regime [5]. These experiments, accompanied by computer simulations, suggest that the rate of secondary nucleation depends on the fibril surface coverage (Eq. S10). Such a dependence necessarily implies that the rate determining step, characterized by the highest free energy barrier on the energy landscape, takes place after the monomer adsorption onto the fibril surface. This rate determining step may for instance involve nucleus formation or detachment.

1.5.6   Comment on the lower bound on the nuclei detachment rate

We can provide an estimate for the lower bound of the detachment rate, by considering that any detachment step following the highest free energy point will be characterized by the following properties: 1) the associated free energy barrier cannot be higher than the highest free energy point (16 kJ/mol); 2) the starting point for the detachment step on the free energy landscape has a free energy higher than $\Delta G_{\text{fib}} = RT \ln(c_{\text{crit}}/c) = -12$ kJ/mol (at 1 μM). For these reasons, we obtain an upper bound for the free energy barrier for detachment: $\Delta G^{\ddagger}_{\text{detach}} \leq (16 + 12)$ kJ/mol $= 28$ kJ/mol. The prefactor is obtained from a scaling argument as $A = cDr_{\text{eff}}N_A = 0.018$ s^{-1}. Thus the rate of detachment will be at least $k_{\text{detach}} \geq A \exp(-\Delta G^{\ddagger}_{\text{detach}}/RT) = 2.2 \times 10^{-7}$s^{-1}.

1.6   Appendix: Equivalence between average first exit time and inverse Kramers rate

In this appendix, we review the equivalence between average first exit times from a potential well and the inverse of the associated Kramers rate.

1.6.1   Average first exit time from potential well

We consider the diffusive motion along a one-dimensional double-well potential potential landscape $G(x)$ (Supplementary Fig. 5a). The time it takes for a particle initially at x_1 to exit the potential well for the first time is denoted with $\tau(x_1 \rightarrow x_2) = \tau$. Because sample paths of the particle's motion are random, τ is a random variable. Considering N independent realizations $\tau_1, \tau_2, \cdots, \tau_N$ we define the average first exit time as [9]

$$\langle \tau \rangle = \lim_{N \to \infty} \frac{1}{N} \sum_{n=1}^{N} \tau_n. \tag{S30}$$

Turning to the definition of Kramers rate, we consider a large ensemble of N independent diffusing particles initially inside the well x_1. We expect that the particles will reach a quasi-equilibrium steady state but will leak out slowly across the potential barrier. If particles are introduced in the potential well at the constant rate J (flux), then the escape rate is given by Kramer's formula [9]

$$r = \frac{J}{p}, \tag{S31}$$

where p is the stationary probability of a particle being inside the potential well. We now show that the Kramers rate can be computed from the average first exit time from the potential well as

$$r = \frac{1}{\langle \tau \rangle}. \tag{S32}$$

Following the approach outlined in Ref. [9], we first notice that if a particle is injected in the well at time $t = 0$ and leaves the well at τ for the first time, then the particle density inside the well evolves as

$$x(t) = \theta(\tau - t), \tag{S33}$$

where θ is the Heaviside step function. Considering now that particles are injected into the potential well at a rate J, then the total number of particles within the well at time t is given by

$$\sum_{n=1}^{N} J \int_0^t \theta(\tau_n - t') dt'. \tag{S34}$$

Hence, the probability that at time t a particle is inside the potential well is given by

$$\lim_{N \to \infty} \frac{1}{N} \sum_{n=1}^{N} J \int_0^t \theta(\tau_n - t') dt'. \tag{S35}$$

Finally, taking the limit $t \to \infty$ (stationary limit), yields the stationary probability of finding a particle inside the well as

$$p = \lim_{N \to \infty} \frac{1}{N} \sum_{n=1}^{N} J\tau_n = J\langle \tau \rangle. \tag{S36}$$

Therefore, from the definition of Kramers escape rate, Eq. S31, we find

$$\langle \tau \rangle = \frac{p}{J} = \frac{1}{r}. \tag{S37}$$

We have therefore demonstrated that Kramers escape rate can be computed by inverting the average first exit time.

References

[1] Kramers, H. A. Brownian motion in a field of force and the diffusion model of chemical reactions. *Physica* **7**, 284 (1940).

[2] Bovier, A., Eckhoff, M., Gayrard, V. & Klein, M. Metastability in reversible diffusion processes. I. Sharp asymptotics for capacities and exit times. *J Eur Math Soc* **6**, 399–424 (2004).

[3] Cohen, S. I. A. *et al.* Proliferation of amyloid-beta42 aggregates occurs through a secondary nucleation mechanism. *Proc Natl Acad Sci U S A* **110**, 9758–9763 (2013).

[4] Meisl, G. *et al.* Differences in nucleation behavior underlie the contrasting aggregation kinetics of the abeta40 and abeta42 peptides. *Proc Natl Acad Sci U S A* **111**, 9384–9389 (2014).

[5] Saric, A. *et al.* Physical determinants of the self-replication of protein fibrils. *Nat Physics* **12**, 874–880 (2016).

[6] Buell, A. K. *et al.* Frequency factors in a landscape model of filamentous protein aggregation. *Phys Rev Lett* **104**, 228101 (2010).

[7] Buell, A. K. *et al.* Detailed analysis of the energy barriers for amyloid fibril growth. *Angew Chem Int Ed Engl* **51**, 5247–5251 (2012).

[8] Zwanzig, R. Diffusion in a rough potential. *Proc Natl Acad Sci U S A* **85**, 2029–2030 (1988).

[9] Reimann, P., Smith, G. J., & Hänggi, P. Metastability in reversible diffusion processes. I. Sharp asymptotics for capacities and exit times. *Phys Rev E* **60**, R1(R) (2004).

2. Supplementary Methods

2.1 Cryogenic transmission electron microscopy.

Cryogenic transmission electron microscopy was used to provide an estimate of the average length, $L(0)$, of the pre-formed fibrils formed at 36°C, which were used in the experiments in Fig. 2, as well as the average length of fibrils formed in reactions at other temperatures. To ensure a stable temperature and to avoid the loss of solution during sample preparation a controlled environment vitrification system was used. Samples were prepared as thin liquid films (<300 nm thick) on glow-discharge treated lacey carbon film coated copper grids and plunged into liquid ethane at -180°C. In this way the original microstructures are preserved as component segmentation and rearrangement is avoided in addition to water crystallisation as the samples are vitrified. Samples were stored under liquid N_2 until measured and then transferred using an Oxford CT3500 cryoholder and its workstation into the electron microscope (Philips CM120 BioTWIN Cryo) equipped with a post-column energy filter (Gatan GIF100). An acceleration voltage of 120kV was used and images were recorded digitally with a CCD camera under low electron dose conditions.

It is interesting to note that the average fibrillar length, $L(0)$, appears only as a multiplicative pre-factor to the elongation rate constant (k_+) in the kinetic equations, i.e. $k_+/L(0)$. Therefore, when substituted into the Arrhenius equation, the average length affects only the pre-exponential factor and hence has no impact on the gradient of the Arrhenius plot. Correspondingly, $L(0)$ has no impact on the activation enthalpies. However, $L(0)$ does enter into the expressions for the activation free energies and entropies but the dependence is logarithmic and therefore weak; for example, the change in the activation free energies and entropies corresponding to a factor of 2 change in $L(0)$ would be $RT \log(2) = 1.7$ kJ mol^{-1}, indicating that experimental error in the determination of the average length does not significantly impact the values reported for the activation energies and entropies.

2.2 Differential centrifugal sedimentation.

Freshly isolated 15μM Aβ42 monomer in 20 mM sodium phosphate, 0.2 mM EDTA, 0.02% sodium azide, 6μM ThT, pH 8.0 was incubated in 96-well half-area plate of black polystyrene with a clear bottom and PEG coating (Corning 3881, Massachusetts, USA), 100 μL per well, in a temperature controlled plate reader (Fluostar OPTIMA and CLARIOSTAR, BMG labtech) until the ThT fluorescence reached a stable plateau. Since the plate reader is only able to hold a stable temperature above the surrounding temperature, for fibril formation at temperatures lower than room temperature, the plate reader was placed in a cold cabinet at 6°C. The contents of each well were injected after vigorous mixing into a 4-12% sucrose gradient in a CPS Disc Centrifuge (CPS Instruments, model 24000 UHR) operated at 24000 rpm. Each presented curve is an average over six replicates. Since the exact sedimentation coefficients differ between each repeat experiment, linear interpolation was used in order to enable averaging of the data sets.

The sedimentation coefficient is a monotonically increasing function of fibril length and hence reports on the size distribution of the fibrils generated in the aggregation reaction. The kinetic theory predicts that the mean fibrillar length at the end of the aggregation reaction, μ, depends on the ratio of the elongation to secondary nucleation rate constants [3], $\mu \sim k_+/\sqrt{k_+ k_2} \sim \sqrt{k_+/k_2}$. Since the rate constant for elongation, k_+, increases at higher temperatures, and the secondary nucleation rate constant, k_2, decreases at higher temperatures, the mean length of fibrils generated is predicted to increase at higher temperatures.

2.3 Data analysis.

As discussed in the main text, the experimental data shown in Fig. 1 were collected in parallel, since the analysis is reliant upon an accurate knowledge of the relative monomer concentrations between

each experiment. It was observed that the absolute noise level in our experimental data increased at lower monomer concentrations, since a fixed level of noise, for example in the initial concentration of peptides or fluctuations in the experimental conditions, is translated into larger absolute errors in the reaction profiles at lower concentrations.

2.4 Glossary.

2.4.1 Kinetic parameters

k_+: Elongation rate constant [units $M^{-1}s^{-1}$].

k_n: Primary nucleation rate constant [units $M^{-(n_c-1)}s^{-1}$].

k_2: Secondary nucleation rate constant [units $M^{-n_2}s^{-1}$].

n_c: Reaction order of primary nucleation with respect to the monomer concentration.

n_2: Reaction order of secondary nucleation with respect to the monomer concentration.

m_{tot}: Total concentration of monomeric peptide [units M].

2.4.2 Thermodynamic parameters

Enthalpy of activation, $\Delta H^{\ddagger}$: The enthalpy difference between the highest point in the energy landscape and the starting point at the same temperature and pressure. It expresses the dependence of a rate constant k on temperature T according to $\Delta H^{\ddagger} = -R\partial \log k/\partial(1/T)$ where R is the gas constant.

Free energy of activation, $\Delta G^{\ddagger}$: The (Gibbs) free energy difference between the highest point in the energy landscape and the starting point. It defines the reaction rate constant k through the Arrhenius equation, $k = A\exp(-\Delta G^{\ddagger}/RT)$, where A is termed the exponential pre-factor or frequency factor.

Entropy of activation, $\Delta S^{\ddagger}$: The entropy difference between the highest point in the energy landscape and the starting point, at the same temperature and pressure. It is calculated from the experimental rate constant k through the relationship $\Delta G^{\ddagger} = \Delta H^{\ddagger} - T\Delta S^{\ddagger}$.
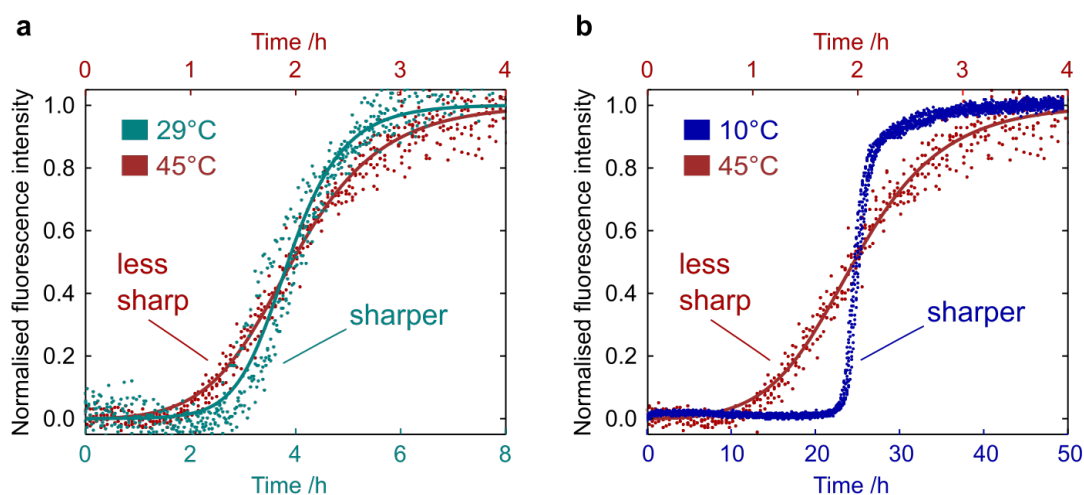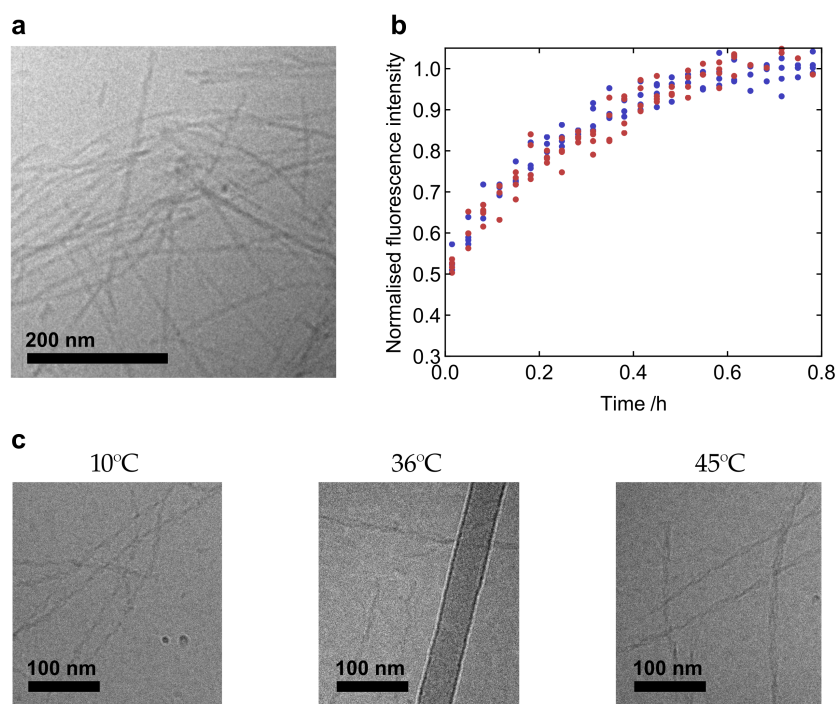
3. Supplementary Figures

3.1 Supplementary Figure 1
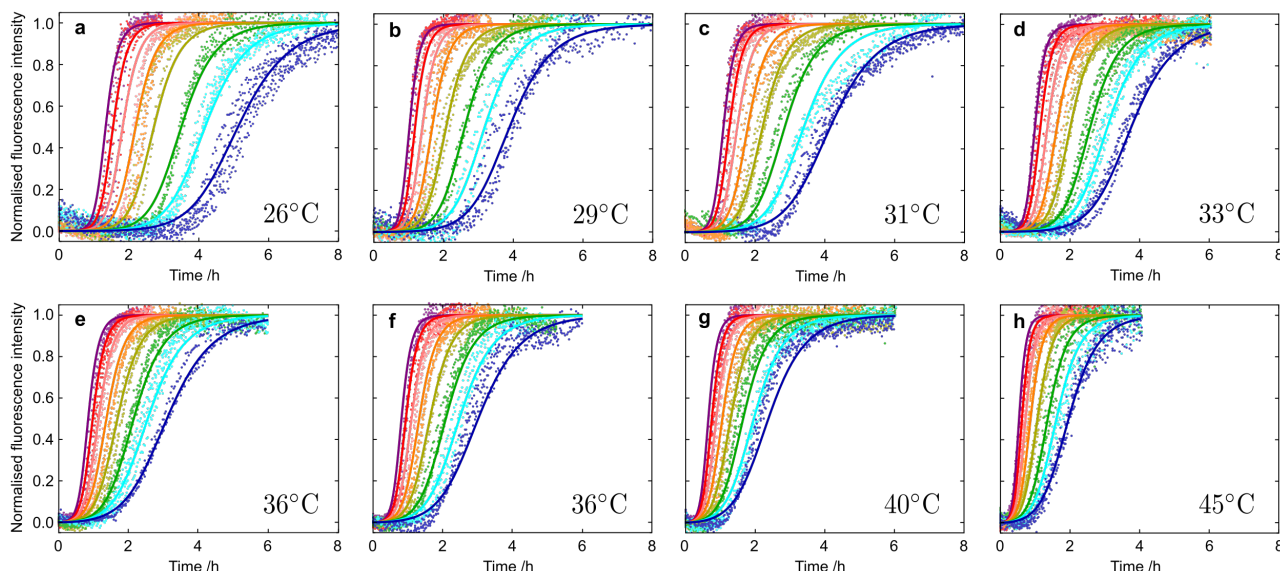
Supplementary Figure 1: Normalized experimental reaction profiles, monitored by ThT fluorescence, for Aβ42 aggregation from purely monomeric peptide for different initial concentrations of monomeric peptide and at different temperatures. The data are the same as those shown in Fig. 1 except that here the scale on the time axes are the same for each panel.
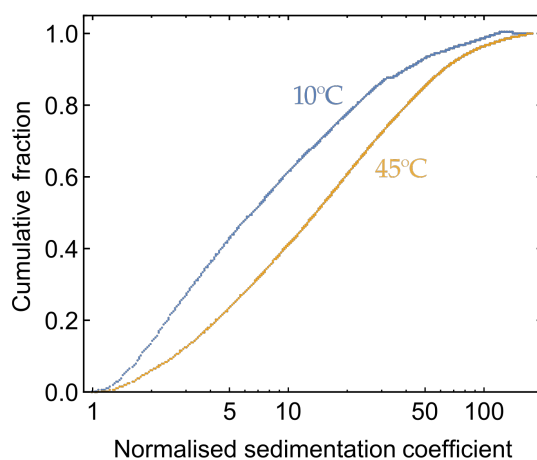
3.2 Supplementary Figure 2

Supplementary Figure 2: Comparison of the shape of the kinetic profiles at **(a)** 29°C and 45°C and **(b)** 10°C and 45°C, for c = 2 μM, showing the reduction in the sharpness of the transition with temperature. Note the different time axes. This macroscopic observation corresponds to a microscopic change in the ratio of the primary nucleation to the secondary nucleation rate constant (i.e. k_n/k_2), which increases as temperature increases (as shown in Fig. 3).
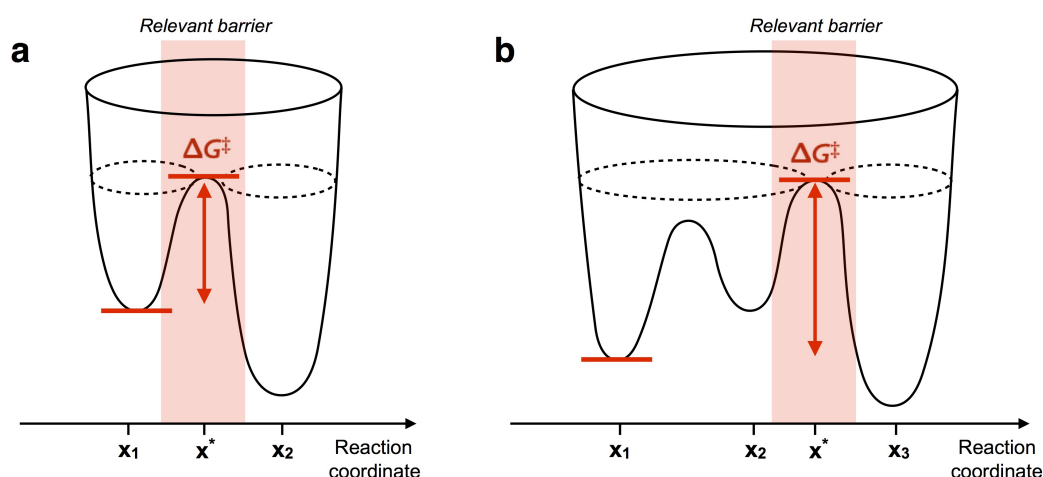
3.3   Supplementary Figure 3

Supplementary Figure 3: **(a)** Representative TEM image, a series of which were used to provide an estimate of the average length, $L(0)$, of the pre-formed fibrils used in the experiments in Fig. 2. **(b)** Normalized experimental reaction profiles for Aβ42 aggregation at 36°C in the presence of 1 monomer equivalent of pre-formed fibrils which had been generated from aggregation reactions at either 29°C (blue circles) or 36°C (red circles), indicating that the temperature at which the pre-formed fibrils were generated does not significantly impact their ability to act as reactive fibril ends. **(c)** Fibril morphologies observed by TEM were similar at all temperatures.
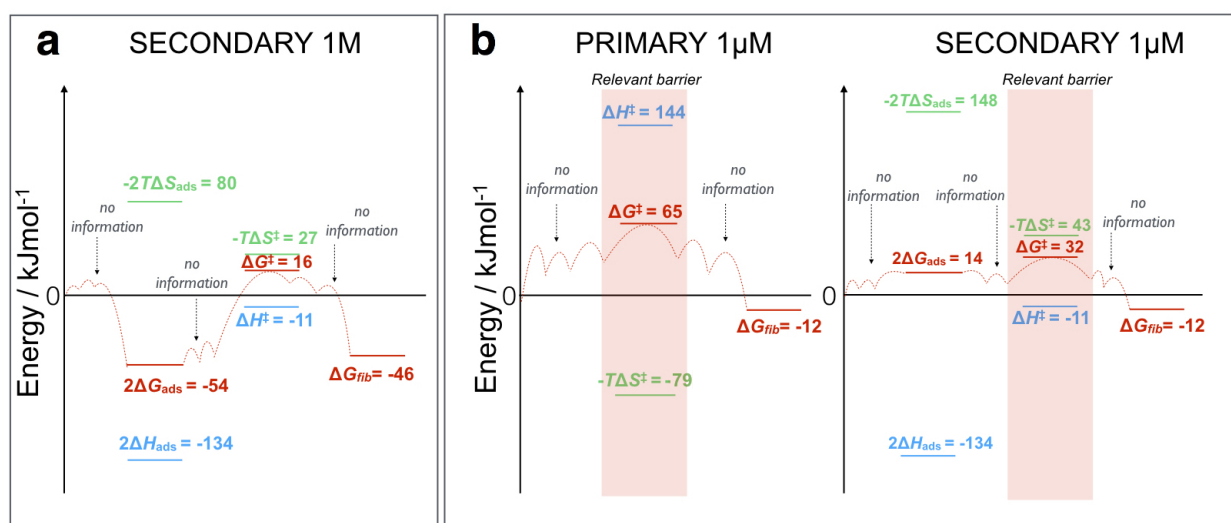
3.4   Supplementary Figure 4

Supplementary Figure 4: Cumulative number distribution of the sedimentation coefficient determined by differential centrifugal sedimentation at different temperatures. Since the sedimentation coefficient reports on fibril length, the data are consistent with the prediction from the kinetic analysis that the mean length of the fibrils generated increases at higher temperatures.

3.5 Supplementary Figure 5

Supplementary Figure 5: Examples of **(a)** double-well and **(b)** multi-well potential landscapes.

3.6 Supplementary Figure 6

Supplementary Figure 6: **(a)** Analysis of the energy contributions of the microscopic steps underlying secondary nucleation at c =1 M and T =298 K. Solid lines represent the quantities directly obtained from our measurements. **(b)** Comparison of energy landscapes underlying primary and secondary nucleation at c = 1 μM and T = 298 K. The relevant barriers are highlighted in a red box, and solid lines represent the quantities directly obtained from our measurements.